Scientific African 20 (2023) e01647

Contents lists available at ScienceDirect

Scientific African

journal homepage: www.elsevier.com/locate/sciaf

Activated cashew carbon-manganese oxide based electrodes for supercapacitor applications

Rebecca Boamah[a], Benjamin Agyei-Tuffour[a], David Dodoo-Arhin[a,b,*], Emmanuel Nyankson[a], Kofi J. Brobbey[c,d], David Obada[e], Latifatu Mohammed[f]

[a] Department of Materials Science and Engineering, University of Ghana, Accra, Ghana
[b] Institute of Applied Science and Technology, University of Ghana, Accra, Ghana
[c] Department of Biomedical Engineering, University of Ghana, Accra, Ghana
[d] Department of Physics, University of Jyvaskyla, Jyvaskyla, Finland
[e] Department of Mechanical Engineering, Ahmadu Bello University, Zaria, Nigeria
[f] Energy Technology Division, Council for Scientific and Industrial Research, Institute of Industrial Research, Accra, Ghana

ARTICLE INFO

Article history:
Received 30 October 2022
Revised 5 March 2023
Accepted 17 March 2023

Editor: DR B Gyampoh

Keywords:
Supercapacitor
Activated carbon
Agrowaste
Characterization
Electrochemistry

ABSTRACT

The current global energy challenge which affects most developing countries in particular, is of major source of concern today. The availability of less expensive techniques of storing excess generated energy is critical to the success of the renewable energy roadmaps implementation. In this study, hydrothermal and chemical leaching methods have been used to synthesize MnO_2 nanoparticles using $KMnO_4$ and $MnSO_4$ as precursors at 140 °C and from natural local manganese ore. Activated Carbon (ACF) have also been produced from agricultural Cashew biomass waste, through a physical carbonization and KOH activation process using temperatures of 700 °C – 900 °C for periods between 1 and 2 h. The as-prepared materials have been characterized via XRD, Raman, FTIR, SEM. Electrochemical performance measurements (CV, EIS and GCD) were carried out on the prepared electrodes. The specific capacitance values obtained were in the range of 2.8 F/g - 6.5 F/g at different scan rates of 20 mV -50 mV respectively in a potential range of -0.4 to +0.4 V and -0.4 to +0.6 V for the various types of electrodes.

Introduction

Over the years, the depletion of fossil fuels, coal etc., have greatly been utilized as global energy demands increases [1]. Due to rapid industrialization, growth in population and technology, energy (electricity) demands have increased over the decades [2]. With the current energy available and grid instability which does not meet the increasing demand results in power fluctuations and outages. Hence, the over-dependence on the conventional fuels (e.g., Fossil fuel) to produce energy for consumption. However, these conventional fuels emits greenhouse gases such as CO_2, which causes environmental degradation and is detrimental to human health and climate changes [3]. Owing to this problem, great demands for re-

* Corresponding author at: Department of Materials Science and Engineering, University of Ghana, Accra, Ghana.
E-mail address: ddodoo-arhin@ug.edu.gh (D. Dodoo-Arhin).

https://doi.org/10.1016/j.sciaf.2023.e01647

newable energy have become a need in the society, which has now become essential that new, clean, low-cost, long term performance, easily portable and environmentally friendly energy storage materials be found in response to these challenges [4,5]. For many years now, considerable efforts have been made to develop new energy materials and storage devices with high energy and power density to meet the world's demand for clean, affordable and sustainable energy [6]. Li-ion batteries and supercapacitors are amongst the potential energy storage devices that have received great attention over these past few years [7]. However, batteries are less considered since its power density, charge-discharge rates, cycle life are limited. Recently, much interest has been shown in considering supercapacitors as one of the most effective energy storage systems due to their high power capability (up to 10 kW/kg), long cycle stability, low cost and environmental friendliness [8].

To overcome the environmental concern and cost constraints, waste or by-products derived from natural products can provide an alternative to the electrode material used for renewable energy storage. In recent years, activated biochar carbon has earned extensive attention for supercapacitor investigation works [9]. Considering the supercapacitor industry, the introduction of renewable biochar to prepare carbon electrode is a cost effective and eco-friendly [9]. Metal/metal oxides are another class of pseudo capacitive materials applicable for developing supercapacitor [10,11].

This preliminary studies focused on the use of prepared activated carbon from Cashew fruits and MnO_2 nanoparticles prepared from both the natural ore (Wassa Nsuta, manganese carbonate ore) via chemical leaching and chemical reactions ($KMnO_4$ and $MnSO_4$) to fabricate a half cell supercapacitor electrode. The electrode materials were characterized via x-ray diffraction (XRD), Fourier transform infrared spectroscopy (FTIR), and scanning electron microscopy (SEM); whiles the electrochemical performance studies (CV, GCD, EIS) of the prepared electrodes were conducted in 3 M KOH electrolyte solutions to measure the supercapacitor variables and to diagnose its performance.

Experimental

Materials and methods

Materials

The manganese ore was obtained from the Nsuta Wassa deposit site in the Wassa West District of the Western Region of Ghana, Cashew fruits (CF) were collected from the University of Ghana farms, Ferrocene, 1-methyl-2-pyrrolidinone (NMP), Polyvinylidene difluoride (PVDF), Potassium permanganate ($KMnO_4$), Manganese Sulphate ($MnSO_4$), Ammonium carbonate (NH_4CO_3), Sulphuric acid (H_2SO_4) and potassium hydroxide (KOH) were purchase from Sigma Aldrich and used without further processing.

Methods

MnO_2 nanoparticles (Hydrothermal approach)and chemical leaching from natural manganese ore. In a typical synthesis process (Fig. 1), 1 g of Manganese Sulfate ($MnSO_4$) was dissolved in 30 ml of deionized water and 1.5 g of Potassium permanganate ($KMnO_4$) was dissolved in 60 ml of deionized water separately. The $MnSO_4$ solution was slowly added to the $KMnO_4$ solution under constant magnetic stirring for 30 min to form a homogeneous mixture. The mixture was then transferred into a 120 ml capacity Teflon-lined stainless-steel autoclave and heated in oven at 180 °C for 8 h. The autoclave was then allowed to cool down to room temperature and the precipitated product filtered and washed several times with distilled water and ethanol via centrifugation at 1000 rpm. Finally, the product was dried under ambient atmosphere in an electric oven at 80 °C for 5 h and labelled **MnO_2-A.**

10 g of manganese ore ($MnCO_3$) was dissolved in 100 ml of 1.8 M dilute H_2SO_4 under constant magnetic stirring for 2 hr at 60 °C. The mixture was then filtered after cooling down to room temperature. 15 g of NH_4CO_3 was then added gradually to the filtrate under constant stirring to precipitate out the $MnCO_3$. The precipitate formed was then washed with deionized water and ethanol solution and then oven dried at 80 °C overnight. The final product was calcined in a temperature controlled muffle furnace at 400 °C for 2 hr to decompose the $MnCO_3$ into MnO_2 particles and labelled **MnO_2-B.**

Conversion of cashew fruits waste to activated carbon. As shown in Fig. 2, cashew fruits (CF) were collected from the University of Ghana farms and washed with distilled water and ethanol to remove the dirt and impurities. The cleaned CF were dried at 100 °C for 36 hrs and grounded into powder using an electric grinding machine. 10 g of the powdered CF was soaked in 100 ml of distilled water containing 10 ml of 0.5 M Sulphuric acid, transferred into a 120 ml stainless steel autoclave unit which was then sealed and heated up to 140 °C for 12 h. The resulting dark-brown product was allowed to cool down to room temperature and was filtered and dried at 80 °C for 24 h and labelled H–CF. The dried product was mixed with potassium hydroxide pellet in different mass ratios using an agate mortar before being carefully transferred into a corundum crucible and placed in a horizontal tube furnace. The furnace was heated at 10°C / min up to 300 °C for the carbonization process under Argon gas atmosphere at flow rate of 600 ml/min for 1 hour and then the samples were activated at a temperature range of 700°C - 900°C for 2 h. The as-prepared carbonaceous materials were washed with a 3 M hydrochloric acid stock solution and distilled water until a neutral pH value was achieved. The samples were dried at 60 °C for 24 hrs in an electric oven for characterization and application.

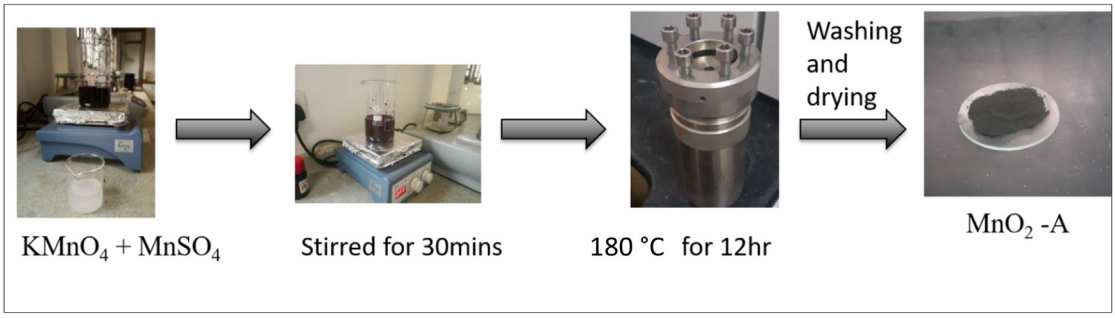

Fig. 1. Preparation of MnO_2-Nps via (**a**) hydrothermal process and (**b**) Chemical leaching from natural ore ($MnCO_3$) powder.

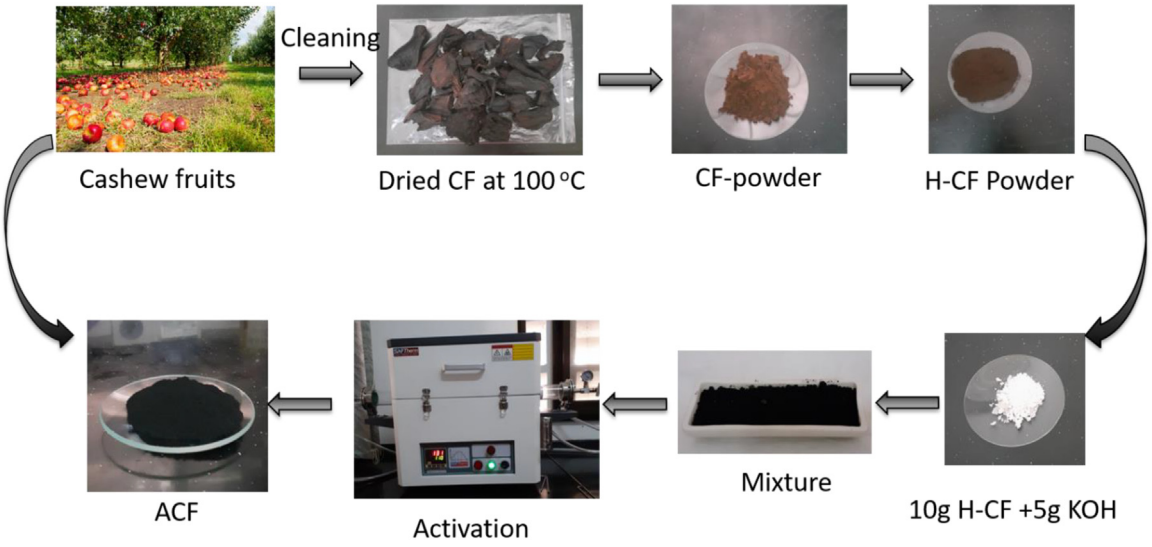

Fig. 2. Preparation of activated carbon from cashew fruit (ACF).

Characterization. X-Ray Diffraction (XRD) was conducted on the prepared samples using Empyrean X-ray Diffraction system with copper (Cu) Kα radiation x-ray tube with a wavelength (λ) = 1.54059 Å at 45 kV and 40 mA for the phases present and the crystallite sizes of the various synthesized nanoparticles and the activated carbon from CF. The XRD pattern of the randomly arranged powder samples was recorded in the 5 °– 85 ° 2θ range with a step size of 0.001°and a count time of 16.575 s per step. The diffraction patterns were matched against the ICSD's PDF database and qualitative phase analysis conducted using the X'Pert Highscore plus search match software (Panalytical, Netherlands). The estimated mean crystallite size of the MnO_2 nanoparticles samples were also calculated from the X-ray diffraction pattern based on the three

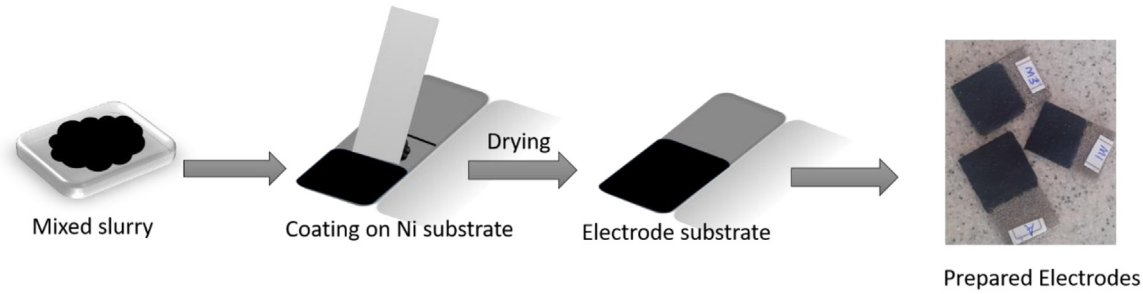

Fig. 3. Preparation of working electrodes.

most intense reflections by using the Scherrer broadening technique [12]. Surface functional groups and molecular bonds existing in the produced samples were conducted using a Perkin Elmer Fourier Transform Infrared (FTIR) spectrometer. Spectra data were recorded and analysed using the Spectrum 10^{TM} software within the 4000 – 450 cm^{-1} spectral range in transmission mode. For the morphological investigations, the MnO_2 nanoparticles were sputtered coated with carbon to make the particles conductive and allow for higher magnifications in a high resolution Zeiss Ultra plus 55 field emission scanning electron microscope (FESEM) which was operated at 2.0 kV

Electrochemical performance studies.

Electrode preparation. In preparing the active electrodes (*Fig. 3*), a nickel foam (Alantum) current collector was used as a substrate. The Ni foam substrate was pre-treated by carefully etching with 2 M HCl in ultrasonic bath for 30 mins to remove oxide layer on the Ni foam substrate surface. After etching, the Ni foam substrate was rinsed in ethanol and deionized water several times in ultrasonic bath and then dried at ambient temperature [13].

In the preparation of the working electrodes, 90 wt% each of the synthesized MnO_2 nanoparticles were mixed with 10 wt% of Polyvinylidene difluoride (PVDF) separately. The mixture was then added to a measured amount of 1-methyl-2-pyrrolidinone (NMP) and then sonicated for 20 mins to form a homogeneous slurry. The slurry was then cast coated on two of the treated Ni foam of dimension 2 cm × 2 cm and dried in vacuum at 80 °C for 6 hrs. The weight of the electrodes were measured before and after deposition to determine the effective material loading. The avearge effective loading of electroactive material was about 0.138 g.

The electrochemical test was carried out on a Metrohm AutoLab PGSTAT204 work station in a 3 M KOH electrolyte solution at room temperature. Cyclic voltammetry (CV) measurements were carried out at a set potential of −0.2 V in a window range between - 0.4 to + 0.6 V at different scan rates. Galvanostatic charge-discharge (GCD) analysis was carried out at a current density of 1 mA (at a current range of 10 mA – 1 mA) for 10 cycles and 50 cycles and Electrochemical Impedance Spectroscopy (EIS) was carried out at a frequency range of 10 mHz to 10^5 kHz at a potential of 0.2 V. These measurements were carried out in a three-electrode system comprising a 3 M KOH electrolyte solution, a reference electrode of Ag/AgCl in a 3 M KCl solution, a glassy carbon counter electrode and the prepared carbon based (MnO_2 – ACF) electrode substrate as the working electrode.

Results and discussion

Synthesis of MnO_2 nanoparticles

Hydrothermal synthesis technique was used for the preparation of the MnO_2 nanoparticles. This technique is based on a controlled precipitation through a closed system heating and formation of solid particles on the transformation of supersaturated to saturated solution state. The MnO_2 nanoparticles was chemically synthesized by using the $KMnO_4$ and $MnSO_4$ in the reaction below;

$$2KMnO_4 + 3MnSO_4 + 2H_2O \rightarrow 5MnO_2 + K_2SO_4 + 2H_2SO_4 \quad (1)$$

The $KMnO_4$ was used as the oxidizing agent which oxidizes the Mn^{2+} ions from the $MnSO_4$ salt dissolved in the distilled water to form small MnO_2 nanoparticles. The crystallinity of the nanoparticles formed gradually increases with the reaction time. The natural ore obtained from Wassa ($MnCO_3$) was leached with sulphuric acid and ammonium carbonate powder by forming MnO pulp with dissolved CO_2, NH_3 and H_2SO_4 which was dried at 80 °C overnight to obtain the MnO_2 nanoparticles and calcined at 400 °C.

X-Ray diffraction (XRD) analysis

The phase structure of the prepared MnO_2 nanoparticles was examined by XRD analysis setup. Fig. 4 shows the XRD peaks of chemically synthesized MnO_2 nanoparticles (A) with different mass ratios of the precursors used; $KMnO_4$ and

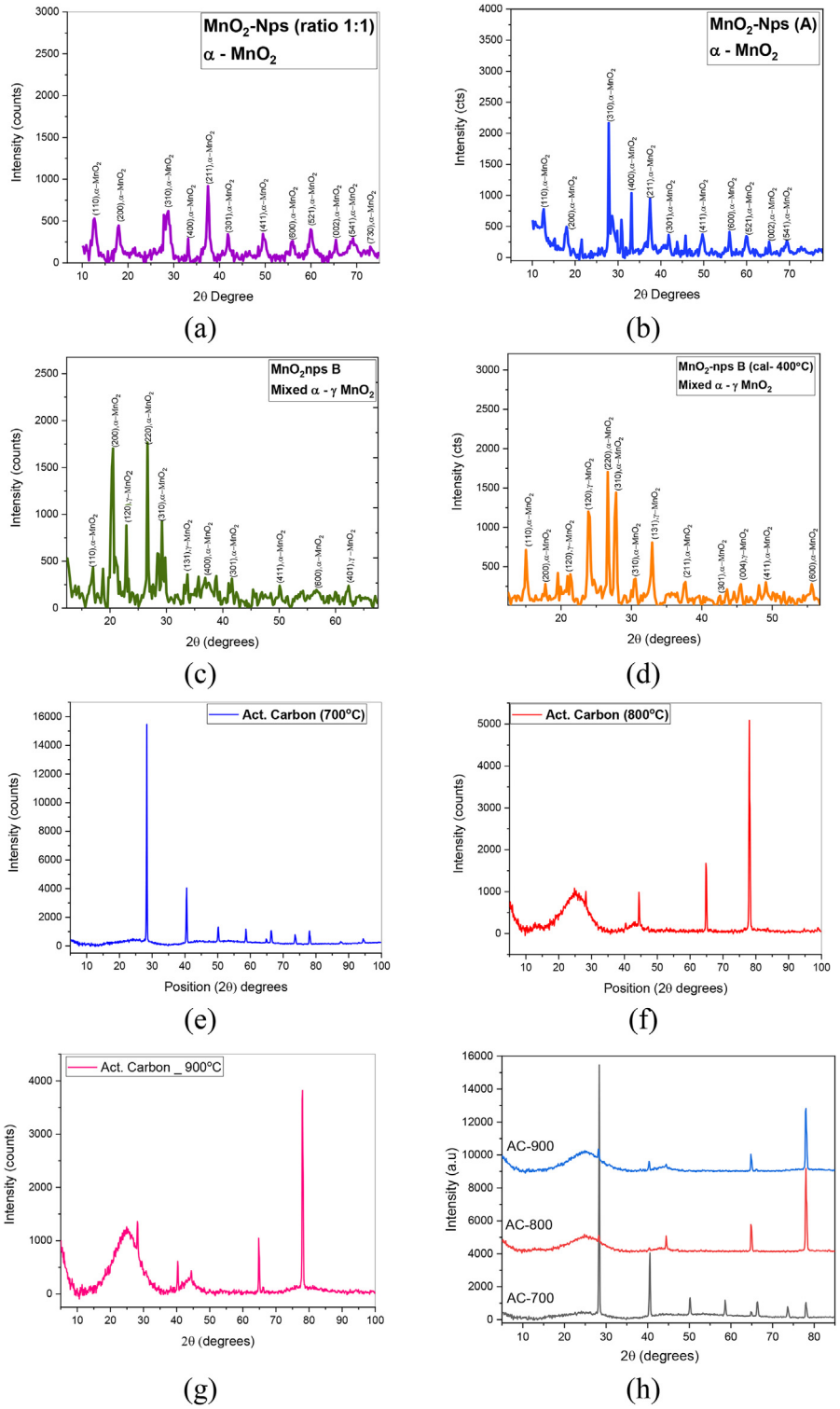

Fig. 4. XRD profile of synthesized MnO_2 with (a) 1:1 & (b) 1:0.5 chemical reactants mass ratios; leached **(c)** MnO_2 nanoparticles **(d)** calcined MnO_2 at 400 °C; chemically activated carbon at **(e)** 700 °C **(f)** 800 °C **(g)** 900 °C and **(h)** compare phase transformation.

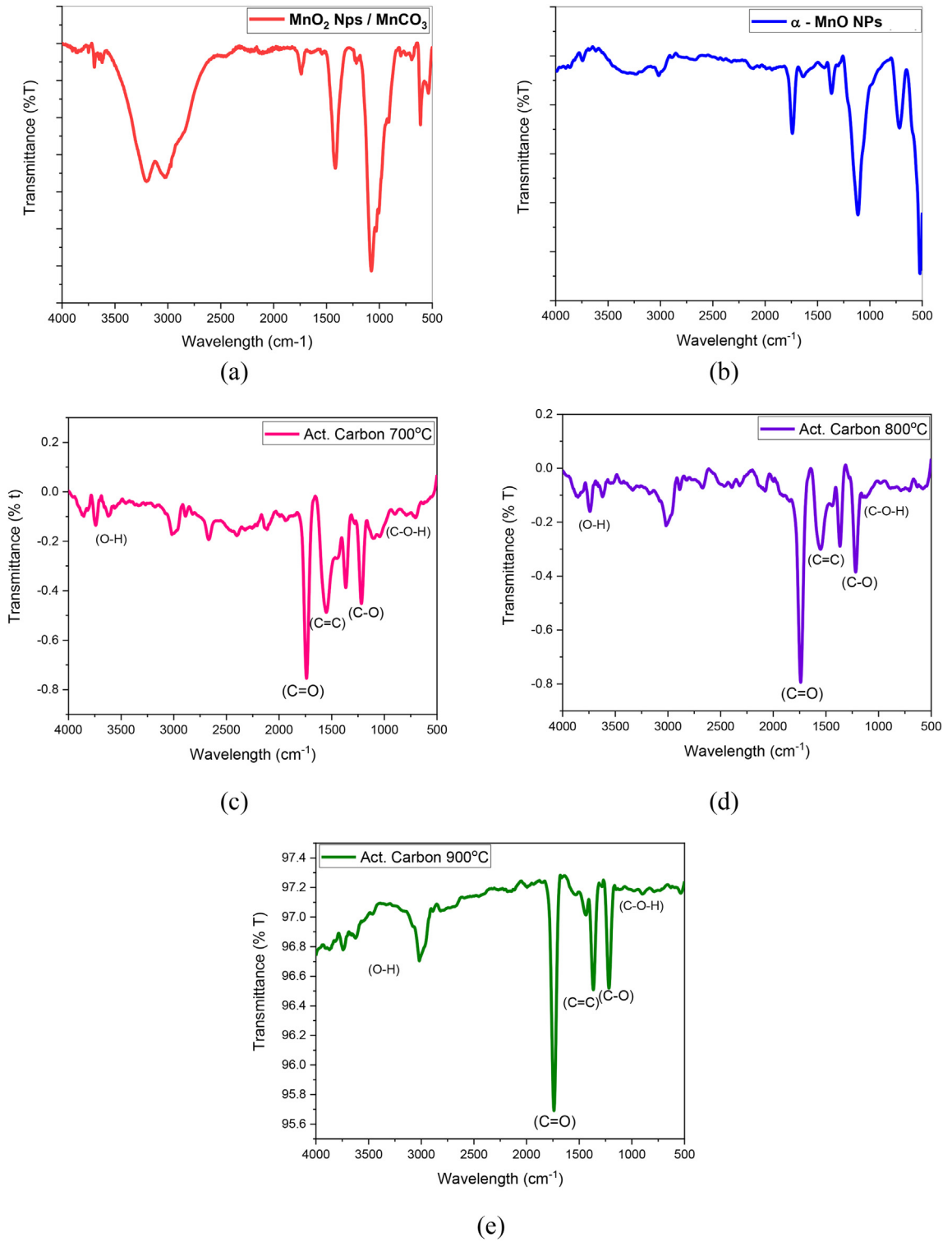

Fig. 5. FTIR spectroscopy (a) leached MnO_2 nanoparticles (b) chemically synthesized MnO_2 NPs and prepared cashew activated carbon at (c) 700 °C (d) 800 °C (e) 900 °C.

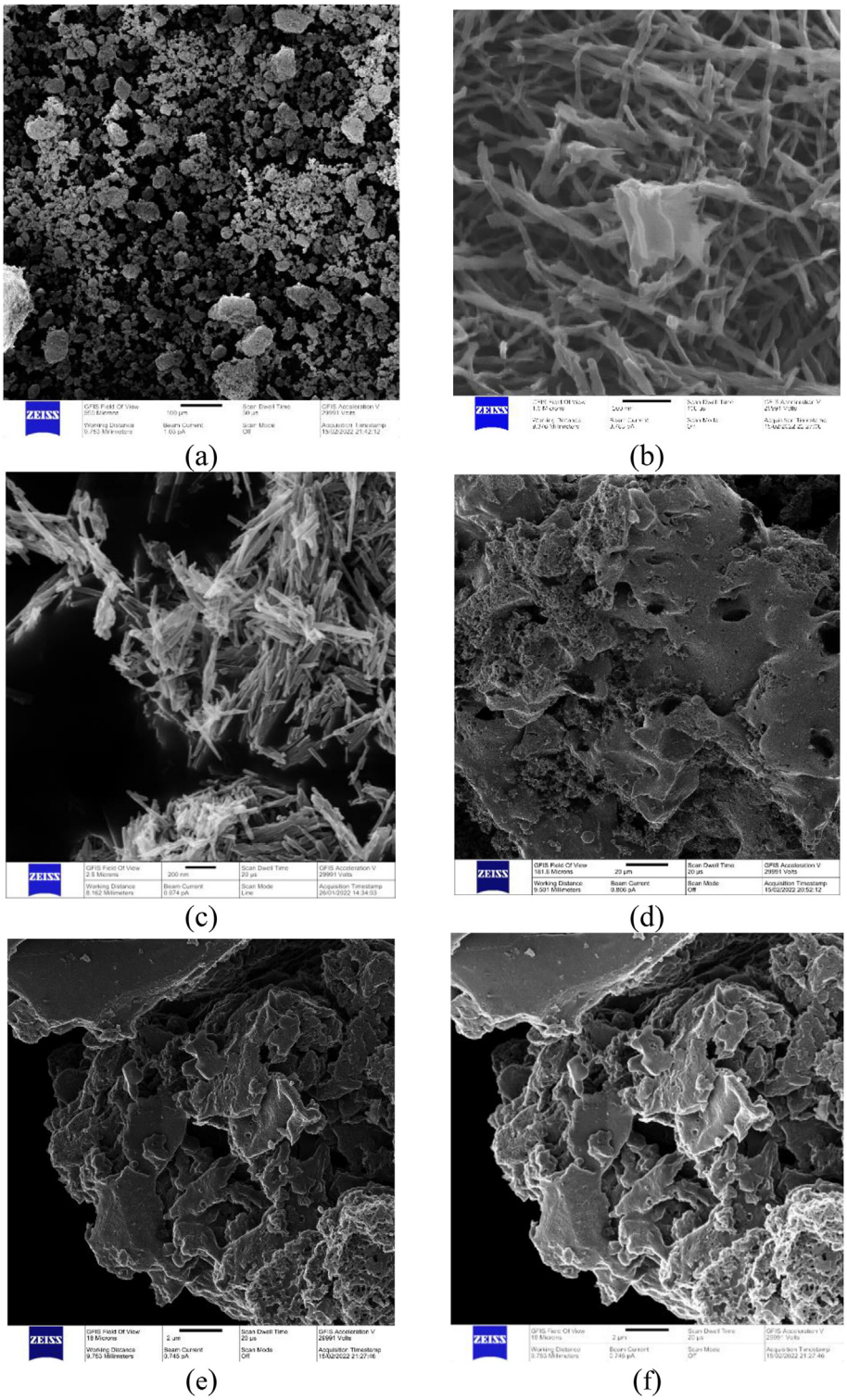

Fig. 6. Scanning Electron microscopy of (a) Manganese ore, (b) leached MnO_2 NPs, (c) synthesized MnO_2 NP, activated carbon from cashew fruit (d) @ 800 °C, (e) @ 800 °C and (f) @ 900 °C.

$MnSO_4$: **(a)** 1:1 mass ratio **(b)** 0.65:0.5 mass ratio. The identified peaks in both the XRD patterns in Fig. 4**(a)** and **(b)** exhibit tetragonal α-MnO_2 phase. The absence of other manganese oxide phase indicates that the synthesized product is a pure α-MnO_2 nanoparticles with a lattice constant of $a = 0.9785$ nm, $c = 0.286$ nm. The sharp peaks in both graphs indicate good crystallinity of the prepared nanoparticles. However, nanoparticles behaviour is exhibited in Fig. 4**(a)**, since it shows broader peaks compared to that in Fig. 4**(b)**. The calculated crystallite size from the Scherrer's formula [12] $D = \frac{k\lambda}{\beta Cos(\theta)}$ gives 9.9 nm crystal size for the synthesized nanoparticles. Fig. 4**c** also shows the XRD patterns of MnO_2 nanoparticles from the leaching of natural manganese ore ($MnCO_3$).

Fig 4**c** represent the leached MnO_2 nanoparticles produced whiles Fig. 4**d** shows the peaks of the MnO_2 nanoparticles after calcination at 400 °C for 2 h. The evident diffraction peaks with their respective indexes in both graphs shows that of a tetragonal mixed α-γ MnO_2 phase. The intense and sharp peaks show good crystalline nanoparticle. The calculated crystallite size using the Scherrer's formula [12] was 24.3 nm.

The XRD patterns of KOH activated carbon from cashew fruits (ACF) at different temperatures for specified times are presented in Fig. 4**e** ACF 700 °C, Fig. 4**f** ACF 800 °C and Fig. 4**g** ACF 900 °C. The peaks of these activated carbon were matched to that of graphitic ICDS peaks. The high intense diffraction peaks shown in the ACF sample peaks shows the degree of crystallinity of the carbon produced. In Fig. 4(f) and (g) the diffraction peaks at 2θ values of 26 °and 45 ° exhibit graphitic (carbon) peaks which appears amorphous with increasing temperature. The phase transformation with increasing temperature is shown in Fig. 4(h).

Fourier transform infra-red spesctroscopy (FTIR) analysis

Fig. 5**(a)** and **(b)** below shows the FTIR analysis spectra of the leached and chemically synthesized MnO_2 nanoparticles. The broad existing bands around 3250 cm^{-1} to 2950 cm^{-1} range correspond to the O–H stretching vibrational mode of adsorbed water by the MnO_2. The absorption band of the hydroxyl group (-OH) around 3250 cm^{-1} to 2950 cm^{-1} for Fig. 5(a) is broader compared to that in Fig. 5(b). which may be as a result of the leaching chemicals (H_2SO_4, NH_4CO_3) used. The absorption bands around 1750 cm^{-1} to 1300 cm^{-1} also correspond to the C–O groups and the bands below 725 cm^{-1} correspond to Mn-O bending and stretching vibrations. In identifying the functional groups of the activated carbon (ACF), the spectra in Fig. 5(c),(d) and (e), indicates that the spectra for all the samples show similar features with main peaks at 3400 cm^{-1}, 2980 cm^{-1}, 1720 cm^{-1},1600 cm^{-1}, 1100 cm^{-1} and below 1000 cm^{-1}.

The absorption bands around 3700 cm^{-1} to 3400 cm^{-1} correspond to the O–H strecthing of hydroxyl functional groups found in all activated carbon materials. The bands at 1720 cm^{-1} correspond to the C = O groups, 1600 cm^{-1} correspond to the C = C stretching functional groups and 1100 cm^{-1} and below 1000 cm^{-1} correspond to the carboxylic group C–O stretching vibrational bonds. The high intensity peaks in Fig. 5**(e)** can be related to the time used for the activation of the carbon with less amount (4 g) of KOH.

Scanning electron microscopy (SEM) analysis

The morphological information on the as-prepared MnO_2 nanoparticles and the activated carbons at various temperatures are presented in Fig. 6. From Fig. 6b, the leached manganese oxide from the primary ore shows a network of wire-like nanostructures while the manganese oxide produced via the hydrothermal route (Fig. 6c) tend to show distinct needle-like nanostructures. These observations are consistent with studies by Dawadi et al. who studied the various synthesis, application and challenges of Manganese dioxide nanoparticles [14].

The SEM image of the activated carbon samples (Fig. 6d,f) showed rough surfaces and evidence of porosity. The porosity of activated carbon products could be attributed to the decomposition of lignin, cellulose and hemicellulose during the carbonisation process, resulting in the formation of microporous and mesoporous structures [15].

It is worth stating that, for energy storage applications, highly porous electrode materials are preferred, of which carbonaceous materials are the industry lead. High porosity not only creates the high surface area, but also allows excellent wettability of the electrode with the chosen electrolyte [16]. The porosity and conductivity effect is also evident in the electrochemical performance of the studied electrodes. Although the activated carbon samples showed porous crystalline structures at lower temperatures, at higher temperature of 900 °C, they tend to be more amorphous. This is consistent with the observations from the XRD data within the 10 –30° 2 theta angles.

Cyclic voltammetry analysis

The Cyclic Voltammetry measurements (*Fig. 7*) for the synthesized ACF and mixed MnO_2/ACF electrodes were carried out in 3 M KOH electrolyte solution at different scan rates (10–300 mV/s) at a set potential of −0.2 V in a potential window of −0.4 V to + 0.6 V. The curves shows a symmetric reversible rectangular slopes which correspond to an ideal capacitive behaviour.The upper vertex or peak correspond to the oxidation peak and the lower vertex correspond to the reduction peak. The ACF electrodes in Figs. 7(g), (h) and (i) exhibit a rectangular slope with a slight distortion as the activation temperature increases but maintains its shape which indicates an excellent rate capability (*ability to generate a considerable amount of power, even at high current loads*), fast ion or charge transfer and Electrochemical Double Layer Capacitor (EDLC) behaviour. In electrochemical double layer capacitors, energy storage arises from the accumulation of electronic and ionic charges at the

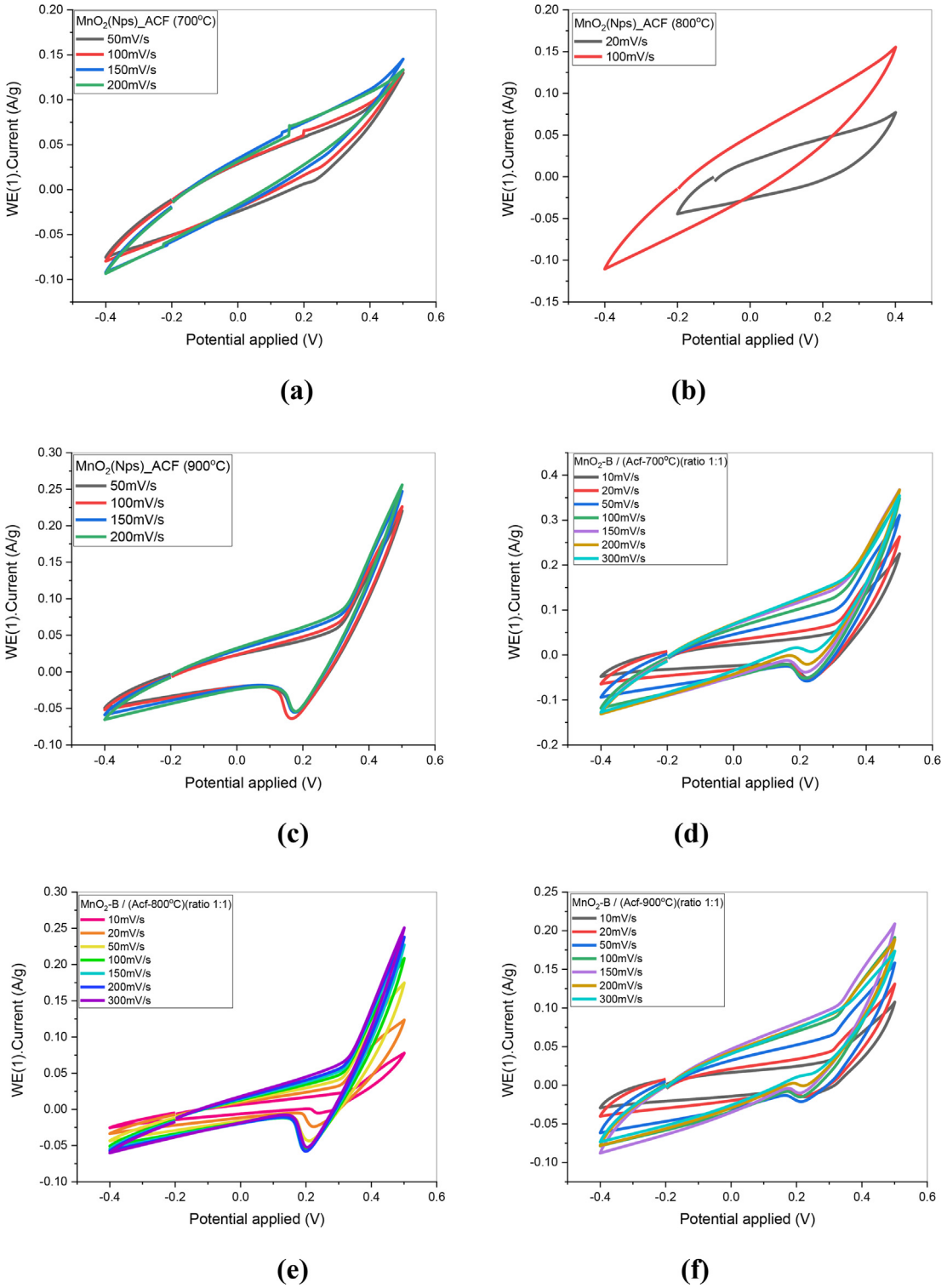

Fig. 7. Shows the Cyclic V curve graphs for synthesized, activated carbon (ACF at 700 °C, 800 °C and 900 °C) and mixed MnO_2 nanoparticles (MnO_2 Nps - A, MnO_2-B) with ACF at different scan rates.

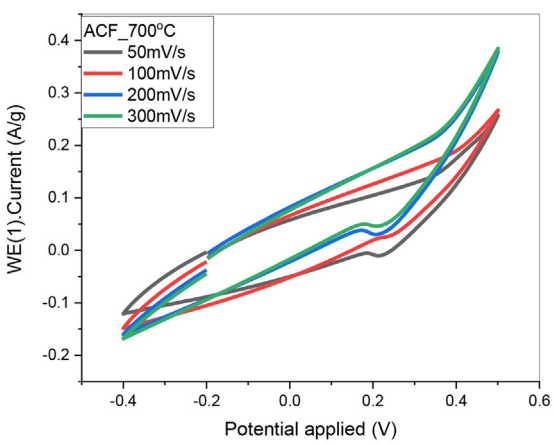

(g)

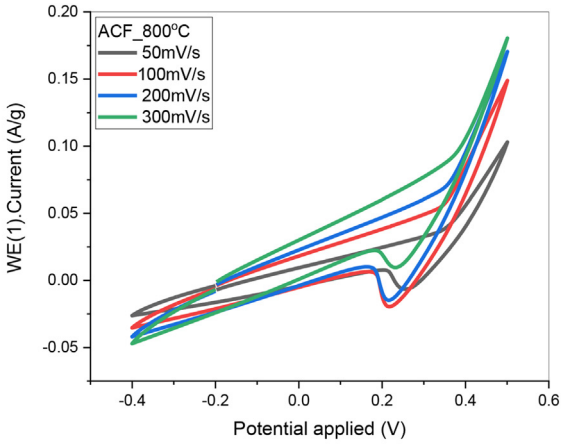

(h)

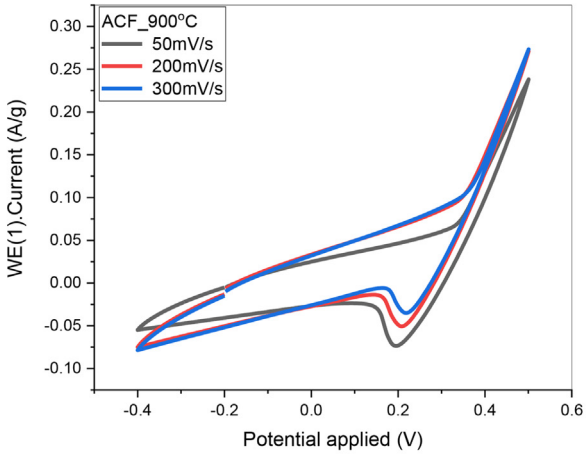

(i)

Fig. 7. Continued

interface between the electrode materials and the electrolyte solution. Fig. 7(a) having a mixture of MnO_2-A nanoparticles and ACF-700 °C exhibit a perfect reversible rectangular slope at scan rates from 50 to 200 mV/s. However, with a mixture of ACF-900 °C; Fig. 7(c), the curve distorts slightly but maintains its slope at the different scan rates. Fig. 7: (d), (e), and (f) slopes are that of the leached MnO_2 (B) nanoparticles mixed with ACF (at 700 °C, 800 °C and 900 °C). These curves exhibit a reversible capacitive behaviour similar to that of the ACF slopes with sligth distortion at scan rates from 10 mV/s – 300 mV/s. Generally, increasing the scan increases the area of the curves. The specific Capacitance of the electrodes were calculated using the CV curves using the equation $Cp = \frac{A}{2km(\Delta V)}$, where A is the area, k is the scan rate, m is the active mass of the electrodes and ΔV is the change in the voltage range.

Electrochemical impedance spectroscopy (EIS) analysis

The electrochemical impedance spectroscopy measurements were carried out at a frequency range of 10 mHz to 10^5 kHz at a potential of 0.2 V at an amplitude of 50 mV. The Nyquist plots show a graph of imaginary impedance (Z_{im}) which correspond to the ability of the electrode to store energy against the real impedance (Z_{Re}) which exhibit the resistance of the flow of charges in the electrode [17]. Figs. 8 shows the impedance plots of MnO_2-A (MnO_2 or MnO_2 Nps), MnO_2-B, ACF and mixed composite (MnO_2/ACF) electrodes. The total resistance exhibited in ACF electrodes in Fig. 8**b** is around 0.8 Ω, that in Fig. 8**c** is around 1.0 Ω and 0.8 Ω for MnO_2 (B)_ACF 700 °C and MnO_2(B)_ACF 800 °C and 900 °C respectively and that of Fig. 8**d** (MnO_2_ACF) exhibit the same resistance value as that of Fig. 8c. In general, due to the presence of the

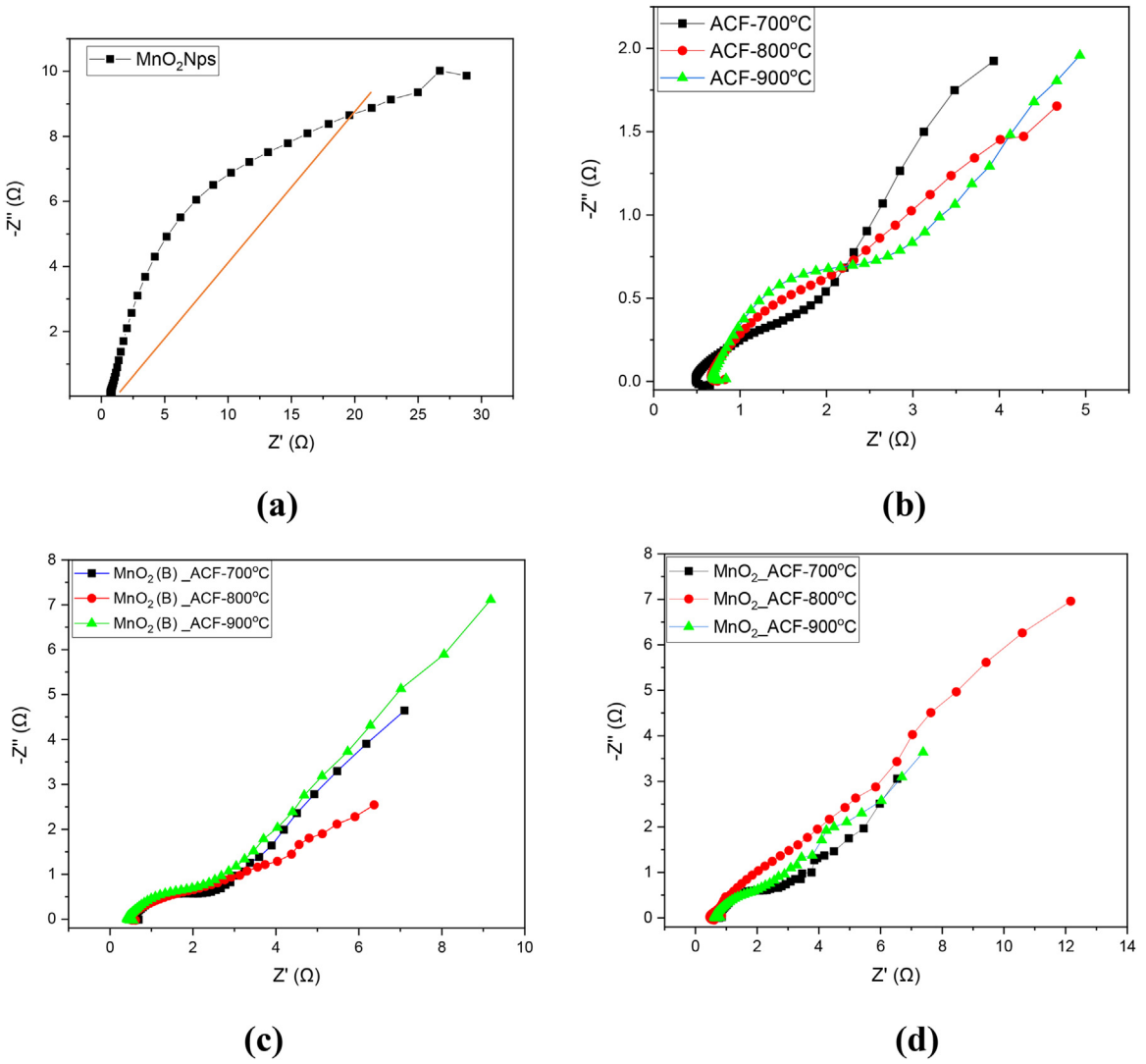

Fig. 8. Shows impedance spectroscopy graphs of synthesized MnO_2 Nps (a), activated carbon (ACF at 700 °C, 800 °C and 900 °C) (b) and MnO_2_ACF (c and d).

highly conductive carbon material in the mixed composite or hybrid electrodes, the resistance to the flow of charges in the electrodes are lower with high electrical conductivity compared to that of the high resistance in Fig. 8a, which is around 1.3 Ω.

Galvanostatic charge-discharge (GCD)

Galvanostatic charge-discharge (GCD) measurement was carried out at a current density of 1 mA (at a current range of 10 mA – 1 mA) for 10 cycles and 50 cycles at a time pf 20 and 100 s respectively for the **MnO_2- A, MnO_2-B (from Ore)** nanoparticles, **ACF** and mixed composite or hybrid electrodes **MnO_2_ACF**. The constant current GCD curves show peaks that go up representing the charging time and the peaks down the discharging time. It can be seen from charge-discharge curves (Fig. 9a-c) that they are nearly linear and symmetrical. The negligible voltage drop indicates that the electrodes have low internal resistance. In addition, the charge-discharge duration for MnO_2-ACFs composites are greater than that of MnO_2 nanoparticles alone, indicating higher specific capacitance for MnO_2-ACF composites based supercapacitors.

The enhancement in the specific capacitance are mainly due to the spacer effect of nanoparticles leading to the increase in accessible surface area of the electrolyte and the progressive redox reactions occurring at the surface and bulk of MnO_2 through Faradaic reactions [18].

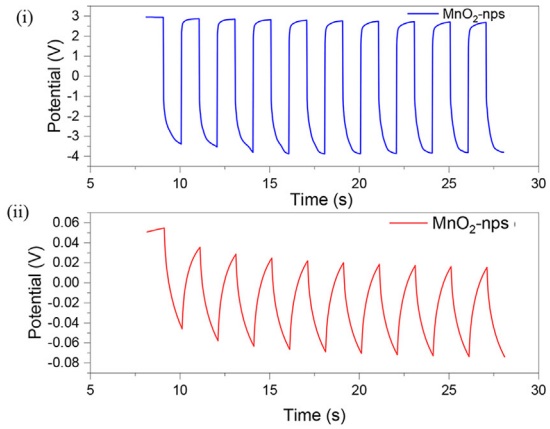

(a)

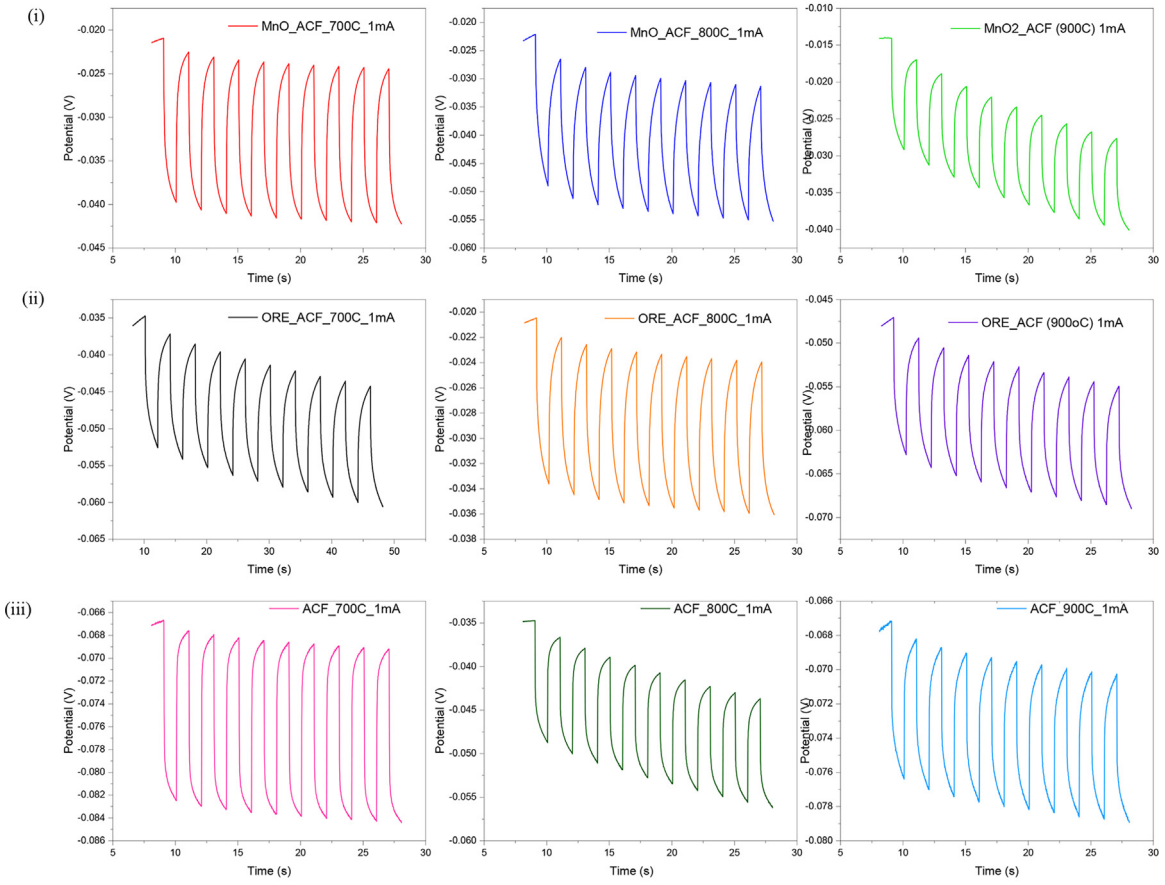

(b)

Fig. 9. Galvanostatic charge-discharge plot of **(ai)** leached MnO_2 and **(aii)** synthesized MnO_2 nanoparticles after 10 cycles; **(bi)** prepared activated carbon (ACF at different temperatures), **(bii)** mixed ACF- MnO_2 nanoparticles and **(biii)** leached MnO_2 (ORE) after 10 cycles; **(ci)** prepared activated carbon (ACF at different temperatures), **(cii)** mixed ACF- MnO_2 nanoparticles and **(ciii)** leached MnO_2 (Ore) after 50 cycles.

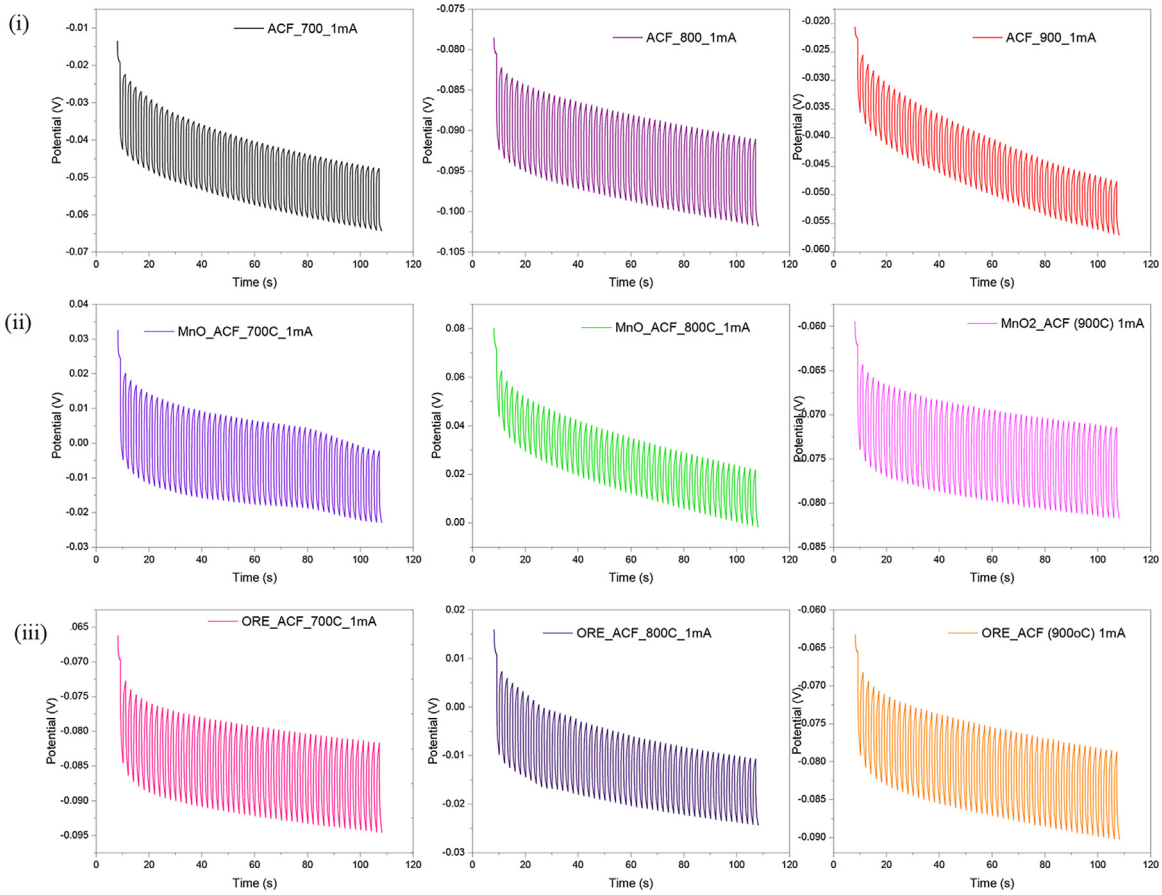

(c)

Fig. 9. Continued

Conclusion

In conclusion, MnO_2 nanoparticles were successfully synthesized by hydrothermal method using chemical precursors and chemical leaching of MnO_2 from natural manganese ore ($MnCO_3$). Also, activated carbon was successfully prepared by KOH activation of carbon from cashew fruits biowaste (ACF). XRD and FTIR techniques were used to analyse the phase structure and the functional groups of the prepared samples. From the XRD analysis, the prepared MnO_2 nanoparticles showed a tetragonal pure α-MnO_2 from the hydrothermal method exhibiting crystallite sizes of 9.9 nm and a tetragonal mixed α-γ MnO_2 phase from the chemical leaching process with a crystallite size of 24.3 nm. The peaks from the ACF prepared matched the standard graphitic or carbon peaks exhibiting a successfully prepared activated carbon. The electrochemical studies performed exhibited a perfect rectangular CV curve with slight distortions as the ACF temperature increased. The specific capacitance from the CV measurements for MnO_2-(A) /ACF-800 °C, MnO_2-(B) /ACF-900 °C, MnO_2-(B) /ACF-700 °C, MnO_2-(B) /ACF-800 °C and ACF-700 °C were 6.5 F/g, 4.7 F/g, 8.6 F/g, 3.7 F/g and 2.8 F/g at different scan rates of 20 mV, 10 mV,10 mV, 10 mV and 50 mV respectively in a potential range of −0.4 V to +0.4 V for former and −0.4 V to +0.6 V for the rest of electrodes.

Data Availability

All data generated or analysed during this study are included in this published article (and its supplementary information files).

Declaration of Competing Interest

The authors declare that they have no known competing financial interests or personal relationships that could have appeared to influence the work reported in this paper.

Acknowledgement

Authors acknowledge support from the University of Ghana Carnegie Corporation of New York-Building a New Generation of Academics in Africa (BANGA-Africa) programme.

References

[1] J. Liu, et al., Co_3O_4 nanowire@MnO_2 ultrathin nanosheet core/shell arrays: a new class of high-performance pseudocapacitive materials, Adv. Mater. 23 (18) (2011) 2076–2081, doi:10.1002/adma.201100058.
[2] Y.S. Li, I.W. Sun, J.K. Chang, C.J. Su, M.T. Lee, Doped butylmethylpyrrolidinium-dicyanamide ionic liquid as an electrolyte for MnO_2 supercapacitors, J. Mater. Chem. 22 (13) (2012) 6274–6279, doi:10.1039/c2jm16391h.
[3] S. Rashidi, M.H. Kashefi, K.C. Kim, O. Samimi-Abianeh, Potentials of porous materials for energy management in heat exchangers – A comprehensive review, Appl. Energy 243 (April) (2019) 206–232, doi:10.1016/j.apenergy.2019.03.200.
[4] S. Rashidi, J.A. Esfahani, N. Karimi, Porous materials in building energy technologies—A review of the applications, modelling and experiments, Renew. Sustain. Energy Rev. 91 (September 2017) (2018) 229–247, doi:10.1016/j.rser.2018.03.092.
[5] S. Rashidi, J.A. Esfahani, A. Rashidi, A review on the applications of porous materials in solar energy systems, Renew. Sustain. Energy Rev. 73 (February) (2017) 1198–1210, doi:10.1016/j.rser.2017.02.028.
[6] Q. Cheng, J. Tang, J. Ma, H. Zhang, N. Shinya, L.C. Qin, Graphene and nanostructured MnO_2 composite electrodes for supercapacitors, Carbon N. Y. 49 (9) (2011) 2917–2925, doi:10.1016/j.carbon.2011.02.068.
[7] H. Wang et al., "Graphene-wrapped sulfur particles as a rechargeable lithium-sulfur-battery cathode material with high capacity and cycling stability."
[8] B. Andres, *Paper-based Supercapacitors*. Mid Sweden University licentiate thesis, Preprints (2014) 112. https://www.diva-portal.org/smash/get/diva2:732015/FULLTEXT02.pdf.
[9] I. Kaushal, S. Maken, A.K. Sharma, SnO_2 mixed banana peel derived biochar composite for supercapacitor application, Korean Chem. Eng. Res. 56 (5) (2018) 694–704, doi:10.9713/kcer.2018.56.5.694.
[10] S. Rashidi, J.A. Esfahani, F. Hormozi, Classifications of Porous Materials for Energy Applications, *Encyclopedia of Smart Materials* 2 (2022) 774–785.
[11] N.E. Ghossein, A. Sari, P. Venet, Nonlinear capacitance evolution of lithium-ion capacitors based on frequency- and time-domain measurements, IEEE Trans. Power Electron. 33 (7) (2018) 5909–5916.
[12] P. Scherrer, Nachr. Ges. Wiss. Göttingen, Mathematisch-Physikalische Klasse, 2 (1918) 98-100.
[13] D. Dodoo-Arhin, R.A. Nuamah, P.K. Jain, D.O. Obada, A. Yaya, Nanostructured stannic oxide: synthesis and characterisation for potential energy, Res. Phys. 9 (2018) 1391–1402.
[14] S. Dawadi, A. Gupta, M. Khatri, et al., Manganese dioxide nanoparticles: synthesis, application and challenges, Bull. Mater. Sci. 43 (2020) 277, doi:10.1007/s12034-020-02247-8.
[15] J. Deng, T. Xiong, H. Wang, A. Zheng, Y. Wang, Effects of cellulose, hemicellulose, and lignin on the structure and morphology of porous carbons, ACS Sustain. Chem. Eng. 4 (7) (2016) 3750–3756, doi:10.1021/acssuschemeng.6b00388.
[16] N. Hillier, S. Yong, S. Beeby, The good, the bad and the porous: a review of carbonaceous materials for flexible supercapacitor applications, Energy Rep. 6 (Supplement 5) (2020) 148–156 ISSN 2352-4847, doi:10.1016/j.egyr.2020.03.019.
[17] N.H. Kwon, L. Kang-Gyu, H.K. Kim, H. Seong-Ju, MnO_2-based nanostructured materials for various energy applications, Mater. Chem. Front. 5 (2021) 3549–3575.
[18] R.B. Rakhi, W. Chen, D. Cha, H.N. Alshareef, High performance supercapacitors using metal oxide anchored graphene nanosheet electrodes, J. Mater. Chem. 21 (2011) 16197–16204.